SANDIA REPORT
SAND20XX-XXXX
Printed Click to enter a date

Sandia National Laboratories

A New Route to Quantum-Scale Structures through a Novel Enhanced Germanium Diffusion Mechanism

George T. Wang, Ping Lu, Keshab R. Sapkota, Andrew D. Baczewski, Quinn Campbell, Peter A. Schultz, Kevin S. Jones, Emily M. Turner, Chappel J. Sharrock, Mark E. Law, Hongbin Yang

Prepared by
Sandia National Laboratories
Albuquerque, New Mexico
87185 and Livermore,
California 94550

Issued by Sandia National Laboratories, operated for the United States Department of Energy by National Technology & Engineering Solutions of Sandia, LLC.

Available to DOE and DOE contractors from
U.S. Department of Energy
Office of Scientific and Technical Information
P.O. Box 62
Oak Ridge, TN 37831

Telephone: (865) 576-8401
Facsimile: (865) 576-5728
E-Mail: reports@osti.gov
Online ordering: http://www.osti.gov/scitech

Available to the public from
U.S. Department of Commerce
National Technical Information Service
5301 Shawnee Rd
Alexandria, VA 22312

Telephone: (800) 553-6847
Facsimile: (703) 605-6900
E-Mail: orders@ntis.gov
Online order: https://classic.ntis.gov/help/order-methods/

ABSTRACT

This project sought to develop a fundamental understanding of the mechanisms underlying a newly observed enhanced germanium (Ge) diffusion process in silicon germanium (SiGe) semiconductor nanostructures during thermal oxidation. Using a combination of oxidation-diffusion experiments, high resolution imaging, and theoretical modeling, a model for the enhanced Ge diffusion mechanism was proposed. Additionally, a nanofabrication approach utilizing this enhanced Ge diffusion mechanism was shown to be applicable to arbitrary 3D shapes, leading to the fabrication of stacked silicon quantum dots embedded in SiGe nanopillars. A new wet etch-based method for preparing 3D nanostructures for high-resolution imaging free of obscuring material or damage was also developed. These results enable a new method for the controlled and scalable fabrication of on-chip silicon nanostructures with sub-10 nm dimensions needed for next generation microelectronics, including low energy electronics, quantum computing, sensors, and integrated photonics.

ACKNOWLEDGEMENTS

We thank Jeffrey Nelson and Paul Sharps for program management efforts. We acknowledge Joaquín Pizarro for providing scanning transmission electron microscopy simulations and Noah "Toby" Jacobson for helpful discussions. This work was performed, in part, at the Center for Integrated Nanotechnologies, an Office of Science User Facility operated for the U.S. DOE, Office of Science. This work was supported by the Laboratory Directed Research and Development program at Sandia National Laboratories.

CONTENTS

1. INTRODUCTION 11
2. Experimental procedures 13
   2.1. Sample Fabrication and Oxidation 13
   2.2. Sample Analysis – (Scanning) Transmission Electron Microscopy 13
3. Method for damage free TEM analysis of 3D nanostructures 15
   3.1. Motivation 15
   3.2. Damage-free, unobscured TEM Cross-Section Fabrication Method 15
4. Controlled formation of Si quantum dots in SiGe pillars by thermal oxidation 19
   4.1. Introduction 19
   4.2. Si Quantum Dot Formation during Thermal Oxidation 19
   4.3. Investigation of Ge Shell around Si QD 21
   4.4. Strain And Electronic Structure Of Si QDs 21
5. Eluciating the enhanced Ge diffusion mechanism during thermal oxidation of Si/SiGe nanowire-fin structures 25
   5.1. Motivation 25
   5.2. Activation Energy Extractions 25
   5.3. Proposed Mechanism 28
6. A Hypothesis for rapid diffusion near interface as (2+) 33
   6.1. Computational Methods 34
   6.2. The Perfect Crystal 34
   6.3. Neutral Silicon Diffusion 34
   6.4. Migration of the (2+) Silicon Interstitial 35
   6.5. Summary 36

LIST OF FIGURES

Figure 1. Cross-sectional HAADF-STEM images of the Si/SiGe superlattice fin structure (a) before oxidation and (b) after 40 min at 900 °C in O_2, forming lateral Si nanowires in SiGe fins. Brighter areas correspond to SiGe layers, and darker areas correspond to Si layers. The black region surrounding the fin is SiO_2 and protective carbon. 11
Figure 2. Schematic showing possible route to arbitrary shaped, embedded 3D Si nanostructures. 11
Figure 3. Key steps in the lamella fabrication process. Red represents Si, blue represents SiGe, yellow represents SiO2, silver represents FIB Pt, and dark grey represents the TEM grid. 16
Figure 4. Cross-sectional HAADF STEM images of Si/SiGe layered nanopillars imaged after wet etch method. 17
Figure 5. HAADF STEM images of 60 nm diameter SiGe (light grey)/Si (dark grey) pillars after oxidation under flowing O_2 at 900 ºC for A) 0 min, B) 5 min, C) 10 min, and D) 20 min, demonstrating encapsulated Si dots. The top, middle, and bottom Si dot widths in D) are 5 nm, 6 nm, and 11 nm, respectively. E) The Si EDS map corresponding to Figure 6D is shown, highlighting three stacked Si dots. F) A higher magnification of the top Si dot in Figure 1D is shown, with the Ge-rich shell surrounding the Si dot highlighted by black arrows. G) The middle dot of the pillar in 6D with a corresponding graphic shown in H) demonstrates the 3-D layers present in the nanostructure. The oxide has been removed from the Si/SiGe pillars before imaging for increased resolution. 20

Figure 6. Summary results of theoretical calculations for the formation energy of Si QDs with and without the Ge shell. 21
Figure 7. Strain calculations for a range of Si dot sizes using molecular dynamics (MD) and electron energy loss spectroscopy (EELS). A) MD simulations (blue dashed line) and strain calculated from EELS (orange line) show a trend for higher strain as the dot diameter decreases. Computational stress maps for B) a 3 nm wide Si dot and C) a 23 nm wide Si dot reveal higher levels of stress in the smaller Si dot and a fairly even distribution of stress within each QD. 22
Figure 8. EELS data for a range of Si QD diameters encapsulated in SiGe pillars. A) Conduction band DOS for the SiGe pillar and for the Si QD/Ge shell/SiGe pillar nanostructure for varying sizes of Si QD diameters. B) Conduction band DOS for Si QDs with varying sizes are shown, with bulk unstrained Si (Si ref.) and Si0.2Ge0.8 (SiGe) as labeled. The red markers highlight the inflection point of each edge onset. C) The change in energy of the Si L3 edge onset is shown as a function of Si QD diameter (D). 23
Figure 9. The conduction band minimum (CBM) offsets for the Si dot, Ge shell, and SiGe pillar. The shift in the D valleys of the Si dot due to hydrostatic strain is given by the product of the strain and a particular combination of the dilatation ($\Xi_d^{(\Delta)}$) and uniaxial ($\Xi_u^{(\Delta)}$) deformation potentials. The total shift in the energies of bound states in the Si dot is then given by the sum of this strain-dependent shift in the D valleys, the shift in core-level energies due to strain ($\chi\varepsilon$), and the shift due to quantum confinement ($E_C(D)$). Relative offsets from bulk Si for the Ge shell (unknown) and the $Si_{0.2}Ge_{0.8}$ pillar (≈350 meV) are illustrated. 24
Figure 10. (a) cross-sectional STEM image of a multilayered Si/SiGe fin before oxidation and (b) is a zoomed in STEM image of the same fin, showing that there is no Ge lateral diffusion. (c) is a cross-sectional STEM image of a fin after 20 minutes of dry oxidation at 900°C. (d) is a zoomed in STEM image of the same oxidized fin, showing that Ge diffuses down the oxidizing interface. (e) is a lattice STEM image showing the defect-free interface between base Si layer and the laterally diffused Ge. 26
Figure 11. cross-sectional STEM image of the Si/SiGe fin after oxidation at 900°C for (a) 5 mins, (b) 10 mins, and (c) 20 mins. The dashed orange line shows the thickness of the thermally grown SiO_2, the blue line indicates the lateral diffusion width, and the solid gray line shows the lateral diffusion length of the Ge. 26
Figure 12. L: a plot showing the linear relationship between lateral diffusion length and the square root of oxidation time. R: a plot showing the linear relationship between lateral diffusion width and the square root of oxidation time. 27
Figure 13. Arrhenius plot of Ge diffusion down the oxidizing interface (length) and into the fin (width) with activation energies of 1.1 and 1.6 eV, respectively. Ge diffusion into Si data taken from *[33, 34]*. 28
Figure 14. Difference in the lateral diffusion lengths after 10 minutes at 900°C of (a) oxidation in dry O_2 and (b) an anneal under forming gas. 29
Figure 15. Potential mechanisms for Ge diffusion (1) through the fin material, (2) through the bulk oxide, and (3) through the suboxide 30
Figure 16. Schematic of experiment carried out to determine whether Ge diffusion occurred through the suboxide or the crystalline side of the interface 31
Figure 17. STEM images of fins that have been oxidized at 850°C for (a) 24 mins, (b) 48 mins, and (c) 24 mins with a 90s HF etch followed by 24 more mins. 31
Figure 18 – Model for fast diffusion near interface 33
Figure 19 - Stable Si(2+) interstitial defect structures 35

Figure 20. Migration path of the I(2+) 36

This page left blank

ACRONYMS AND DEFINITIONS

Abbreviation	Definition
S/TEM	Scanning transmission electron microscopy
EELS	Electron energy loss spectroscopy
QD	Quantum dot
CBO	Conduction band offset
MD	Molecular dynamics
DFT	Density functional theory
Si	Silicon
Ge	Germanium
EDS	Energy dispersive x-ray spectroscopy
SiGe	Silicon germanium
UF	University of Florida
HAADF	High-angle annular dark-field

1. INTRODUCTION

The next generation of silicon (Si) and silicon germanium (SiGe) microelectronics, including low-power devices, spin qubits for quantum computing, on-chip light sources for integrated all-Si(Ge) based photonics/electronics, and nanoscale sensors, require a scalable method to manufacture quantum-scale structures in the sub-10 nm size regime. However, current top-down lithographic and bottom-up synthesis approaches for making on-chip Si/SiGe-based nanostructures with control over size and placement are challenged by these extremely small dimensions. Recent work done at the University of Florida (UF) revealed a previously undiscovered, extremely enhanced Ge diffusion process along Si/SiO_2 interfaces during thermal oxidation of Si/SiGe superlattice nanofins. This enhanced Ge diffusion enabled the formation of lateral Si nanowires embedded in SiGe cladding as shown in Figure 1. Si nanowires with diameters down to 2 nm were realized, thus opening a new potential approach for the fabrication of sub 10-nm diameter nanowires *[1]*. As these nanowires are encapsulated in single crystal defect free SiGe, strain-related properties such as free carrier mobility can potentially be manipulated in such structures.

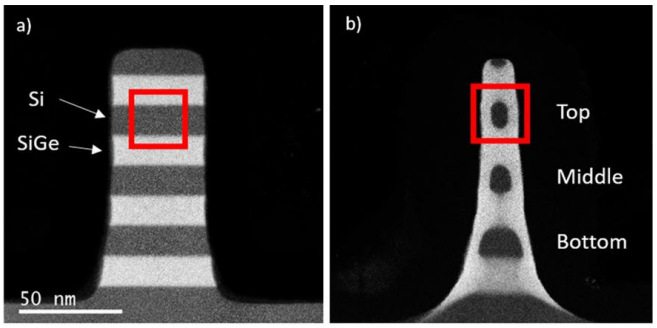

Figure 1. Cross-sectional HAADF-STEM images of the Si/SiGe superlattice fin structure (a) before oxidation and (b) after 40 min at 900 °C in O_2, forming lateral Si nanowires in SiGe fins. Brighter areas correspond to SiGe layers, and darker areas correspond to Si layers. The black region surrounding the fin is SiO_2 and protective carbon.

In addition to nanowires, we propose here that this approach can be applied more broadly to create other, completely novel '3-D' quantum-scale structures such as quantum dots (QDs), toroids, and ellipsoids, which could exhibit unique and useful new properties, and which would not be possible to realize using current approaches (Figure 2). At small enough sizes (e.g. <2.5 nm), Si nanowires have been theoretically predicted to transition from an indirect to a direct bandgap *[2]*. Direct bandgap Si/SiGe quantum-scale structures could enable a host of integrated all Si(Ge)-based photonics, including on-chip optical sources for interconnects, which is a highly sought-after goal that could eliminate the current need for integrating III-V and Si(Ge) materials and devices.

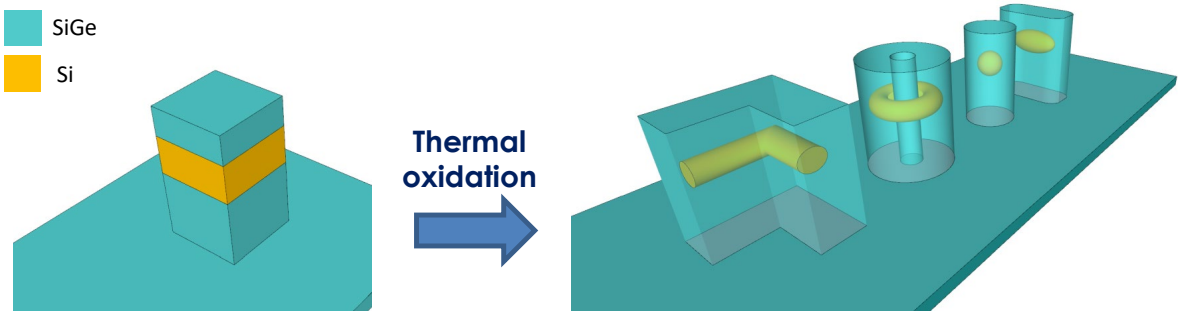

(a) Patterned vertical Si/SiGe nanopillars with custom cross-sections

(b) Vertical SiGe nanopillars with embedded 3D Si quantum structures (shown: L, toroid, dot, ellipsoid)

Figure 2. Schematic showing possible route to arbitrary shaped, embedded 3D Si nanostructures.

This project, in collaboration with the University of Florida (Prof. Kevin Jones and Prof. Mark Law) aimed first to elucidate the mechanism of this novel enhanced Ge diffusion in nanostructures during oxidation, of which little is currently known. Second, we sought to demonstrate that this approach can be extended from the original nanowire-in-fin architecture to arbitrary 3D-shaped embedded nanostructures. This knowledge will be necessary to establish the potential and limitations of this process as a new approach for the controlled and scalable fabrication of on-chip Si/SiGe quantum-scale structures below 10 nm.

To achieve this, the thermal oxidation process was be experimentally studied in 1-D nanopillar and 2-D nanofin structures fabricated from multi-layer Si/SiGe planar material. The fabrication of novel 3-D nanostructures using this approach, including quantum dots and rings was also explored to gauge the potential of this approach to realize a wide range of unique and arbitrary 3-D morphologies for future possible applications. In concert, we investigated theoretical models to understand this enhanced diffusion process and Ge segregation. Our overall goal was to lay the scientific foundation for a powerful new materials capability for creating novel quantum-scale nanostructures en masse with wide commercial and mission relevance for low-energy, beyond Moore's Law electronics (e.g. vertical nanowires), quantum information systems, integrated Si photonics, and beyond.

2. EXPERIMENTAL PROCEDURES

2.1. Sample Fabrication and Oxidation

A single-crystalline, undoped Si/SiGe superlattice was grown on a 300-mm n-type Si(100) wafer with alternating layers of 15 nm-thick Si and pseudomorphic $Si_{1-x}Ge_x$ layers, (x = 0.3). Four layers each of Si and SiGe were grown for a total Si/SiGe stack height of 120 nm, finishing with a Si layer on top. Vertical pillars or fins were defined using e-beam lithography with the nanoscale pattern generation system (NPGS) and using negative photoresist hydrogen silsesquioxane (HSQ). The HSQ was also used as an etch mask for a subsequent continuous Bosch and deep reactive ion etching (DRIE). The continuous Bosch etch provides smooth, nearly vertical sidewalls and shows a selectivity of Si/SiGe:HSQ of approximately 3:1, allowing nanostructures 120 nm in height to be etched with the HSQ mask. Arrays of pillars and fins were fabricated with dimensions ranging from 30 nm to 200 nm in diameter/width in the same pattern, allowing single cross sections to be taken that contained multiple sizes of pillars or fins.

A conventional tube furnace with flowing O_2 was used to oxidize each sample for a different amount of time to create a time series. The targeted temperature for all oxidations, typically 900 °C, was set by an internal thermocouple in the furnace and tested by a secondary thermocouple inserted to the sample location.

2.2. Sample Analysis – (Scanning) Transmission Electron Microscopy

(Scanning) transmission electron microscopy (S/TEM) was extensively used to probe the detailed microstructures of the samples prior to and after thermal oxidation. In particular, high-angle annular dark-field (HAADF) STEM was used to provide Z-contrast imaging whereby Ge appears brighter than Si. High-resolution S/TEM images were taken on a FEI Titan G2 80-200 STEM. Energy dispersive x-ray spectroscopy (EDS) in STEM mode was used to provide chemical composition info.

For the pillars, a new TEM sample preparation method was developed to allow for an unobscured, damage free view of the nanopillars on the original substrate. In this technique, additional deposited oxide protected the pillars during focused ion beam cross-section preparation and allowed for subsequent removal of all material surrounding the pillars using a wet-chemical etch method. This method is described further in Section 3.

3. METHOD FOR DAMAGE FREE TEM ANALYSIS OF 3D NANOSTRUCTURES

Here, we describe a new TEM sample preparation method developed under this project enabling high resolution TEM analysis of 3-D nanostructures free of surrounding material and free of detectable damage. This wet-etch based method enables high quality imaging of the pillar and fin structures with embedded nanostructures studied in this project. Full details have been published in the literature *[3]*.

3.1. Motivation

The characterization of 3-D nanostructures such as those used in quantum emitters, sensing applications, and vertical transistors is problematic due to the nanometer scale size of these structures. This makes it difficult to capture 3-D nanostructures in a focused ion beam (FIB) lift-out lamella without either ion beam damage to the nanostructures during thinning or the unwanted presence of obscuring material in front of and behind the nanostructure. The damage layer introduced to the TEM cross section by the ion beam during thinning of the lamella is one of the universal challenges in FIB lift-out specimens *[4]*. One option is to carefully thin the TEM lamella until it is the thickness of the 3-D nanostructure, removing the material in front of and behind the nanostructure. However, this is difficult for sub 100 nm structures and does not work for circular structures like vertical nanowires, where the edges of the structure will still have unwanted surrounding material. To address this need, this work focuses on the development of a wet-chemical etch process for FIB-processed TEM lamella that leaves 3-D nanostructures free of surrounding material for improved structural analysis.

3.2. Damage-free, unobscured TEM Cross-Section Fabrication Method

Figure 3 illustrates the wet-etch method developed for nanostructure characterization using Si/SiGe pillar arrays (unoxidized) studied in this project an example material. The first step is the deposition of a sacrificial SiO_2 layer as shown in Figure 3B. The SiO_2 layer takes the place of the protective carbon coating often used in situ FIB lift-out methods and provides protection during the initial FIB platinum deposition as well as enabling the later removal of all surrounding material from the cross section. For the 120 nm tall Si/SiGe structures used to demonstrate the wet-etch method, a 200 nm layer of SiO_2 was sufficient to allow for the subsequent chemical etching release without completely removing the sample topography necessary for navigation on the sample during FIB processing. The sample is then ready for cross section fabrication using the FIB, beginning with the deposition of a protective Pt strap as shown in Figure 3C. For the Si/SiGe pillar array, it was useful to deposit the protective platinum and mill out the lamella at a slight angle, ~2-4 degrees, with respect to the pillar rows in order to ensure that a pillar was captured in the lamella. Figure 3D illustrates the necessary TEM grid modifications to ensure a strong lamella attachment to the grid.

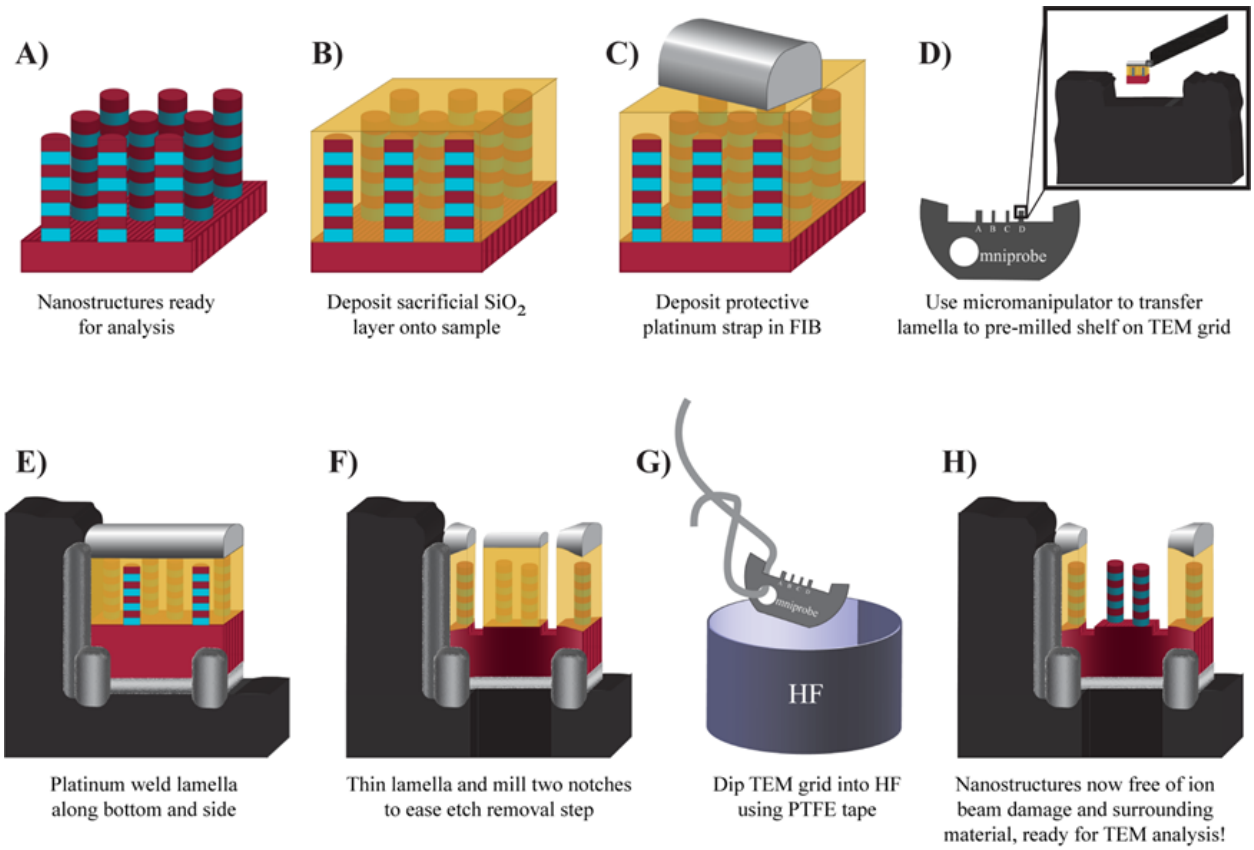

Figure 3. Key steps in the lamella fabrication process. Red represents Si, blue represents SiGe, yellow represents SiO2, silver represents FIB Pt, and dark grey represents the TEM grid.

Once the lamella has been navigated to the corner of the shelf, platinum is deposited to the bottom and side of the lamella nearest the grid shelf as shown in Figure 3E. Once the lamella is securely attached to the grid, thinned to a thickness that ensures only one nanostructure is present for a given thickness of the lamella and notched as shown in Figure 3F, the grid is ready to be wet etched to remove the surrounding material. To secure the grid during the wet etch, Teflon tape string was threaded through the "O" in the grid, creating a large loop with which to securely hold the grid as shown in Figure 3G. The grid was dipped into 49% HF for 30 s followed by a dip into deionized water. Grids were then allowed to dry overnight before TEM analysis. Figure 3H shows the final result of this wet-etch method: 3-D nanostructures free of surrounding material and ready to be analyzed using TEM. Plasma cleaning should be avoided if at all possible after the wet etch of the grid as undesirable deposition of Pt particles was observed on the region of interest after plasma cleaning.

Figure 4 shows Si/SiGe pillars with diameters down to 25 nm to demonstrate this wet-chemical etch method, with Figure 4A illustrating high-angle annular dark-field (HAADF) STEM imaging of a lamella with a range of Si/SiGe pillar diameters. Figure 4A demonstrates the ability to capture a range of nanostructure sizes in one cross section without needing to variably thin the lamella to achieve electron transparency for different nanostructure thicknesses. Figure 4B demonstrates the ability to successfully capture Si/SiGe pillars with diameters down to 25 nm.

Figure 4C provides a high resolution HAADF STEM image of a Si/SiGe pillar sidewall free of surrounding material and free of any damage observable via TEM analysis.

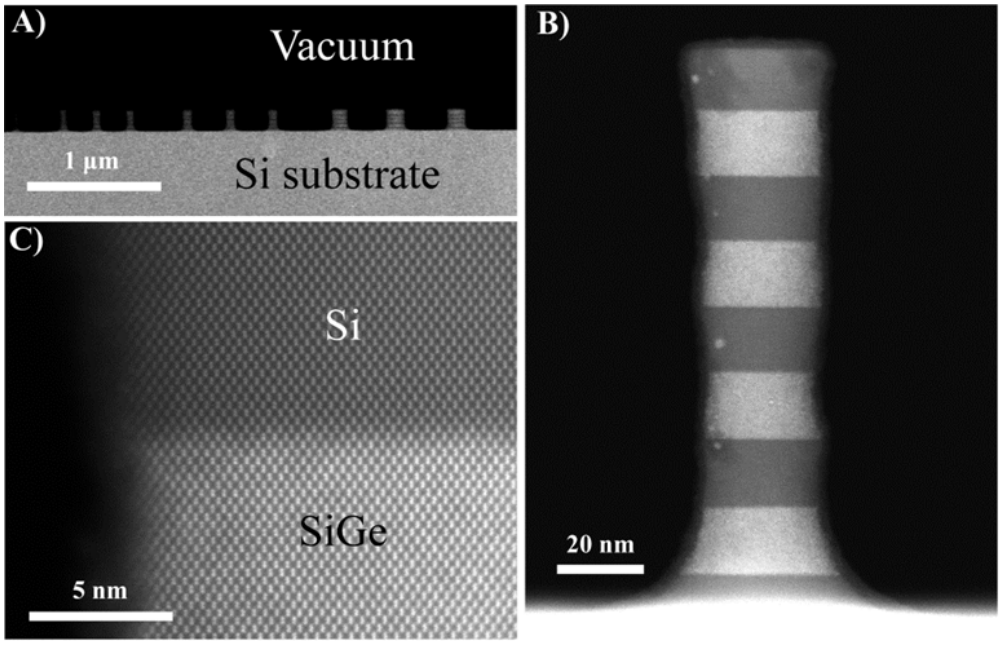

Figure 4. Cross-sectional HAADF STEM images of Si/SiGe layered nanopillars imaged after wet etch method.

4. CONTROLLED FORMATION OF SI QUANTUM DOTS IN SIGE PILLARS BY THERMAL OXIDATION

4.1. Introduction

The ability to fabricate quantum dots (QDs) in a controllable manner compatible with current Si-based manufacturing processes is highly desirable for a wide range of applications including quantum computing, optoelectronics, and microelectronics. Si QDs encapsulated in a SiGe host may be particularly useful for applications reliant on charge trapping. Due to the type-II band alignment between Si and compressively strained SiGe, a Si QD encapsulated in SiGe can achieve quantum confinement for one or more electrons *[5, 6]*, which is desirable for single-electron transistors, single-photon generation/detection, and qubit devices *[5, 2, 7]*. Further, core-shell Si-Ge nanostructures have been shown to offer enhanced performance for a variety of applications *[8-10]*. Here, we demonstrated that the thermal oxidation technique that enables the formation of stacked Si nanowires in SiGe nanofins via rapid Ge diffusion down the oxidizing interface could be extended down a dimension to enable the creation of site-specific, stacked Si quantum dots down to 2 nm in diameter in SiGe nanopillars. Measurements and theoretical calculations of the QD structure, strain and electronic structure were performed. Full details of these results have been submitted for publication elsewhere *[11]*.

4.2. Si Quantum Dot Formation during Thermal Oxidation

Figure 5 shows the evolution of 60 nm-diameter Si/SiGe pillars during oxidation in cross-section using high-angle annular dark-field HAADF STEM images. After a 5-minute oxidation (Figure 3B), a thin SiGe layer forms along the sidewalls of the pillar, resulting in encapsulated Si discs. Increasing oxidation time results in these discs becoming more spherical and decreasing in diameter as shown in Figure 5C. Continued oxidation further reduces the size of these Si dots while still retaining a defined, extended defect-free Si dot interface as shown in Figure 5D. Figure 5E shows STEM energy dispersive x-ray spectroscopy (EDS) Si K mapping of the 20-minute oxidized pillar, highlighting the formation of three stacked, single-crystal Si QDs encapsulated in the vertical SiGe nanowire. With this result, we demonstrate the ability to tune the Si dot size through oxidation time. With continued oxidation, we achieve Si QD sizes down to approximately 2 nm in diameter.

The pillar sidewall shape evolves during oxidation, gradually becoming concave as oxidation time continues and affecting the Si QD dimensions. Previous work studying the oxidation of Si nanopillars revealed slower oxidation rates at the top and bottom of pillars due to curvature effects *[12]*. A similar retardation of the oxidation rate at the top and bottom of the Si/SiGe pillars is observed, leading to encapsulated Si dots that evolve at different rates during oxidation. For example, the top Si dot shown in Figure 5F is slightly larger than the middle dot shown in Figure 5G, likely due to the higher oxidation rate at the middle of the pillar when compared with the top or bottom of the pillar. If necessary, it may be possible to mitigate this effect through a multiple-step oxidation in the self-limiting oxidation regime*[13, 14]* such as that done by Ye et al. to reduce variations in Si nanopillar oxidation *[15]* or by placing the Si layers further from the substrate via a deeper RIE.

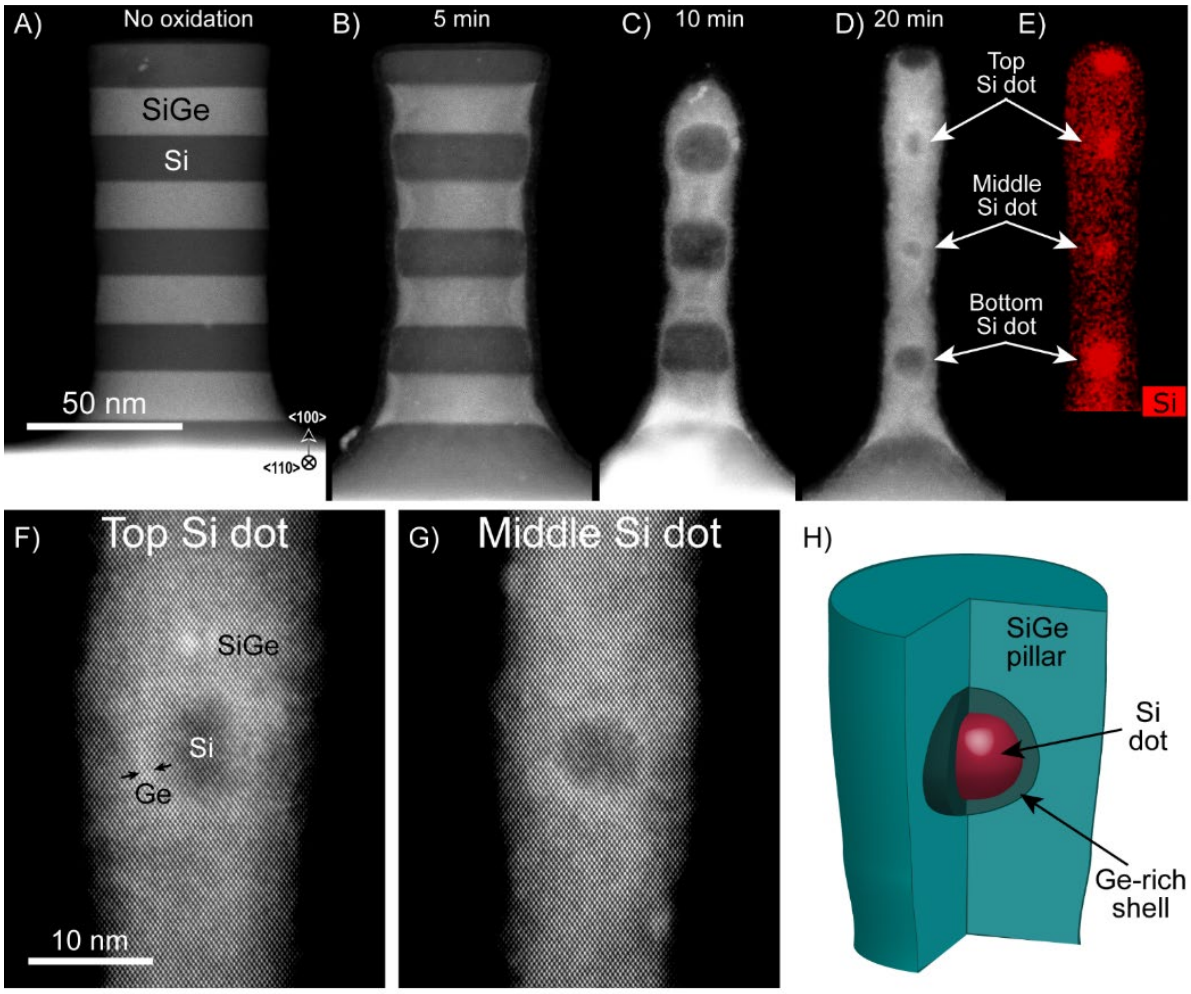

Figure 5. HAADF STEM images of 60 nm diameter SiGe (light grey)/Si (dark grey) pillars after oxidation under flowing O_2 at 900 ºC for A) 0 min, B) 5 min, C) 10 min, and D) 20 min, demonstrating encapsulated Si dots. The top, middle, and bottom Si dot widths in D) are 5 nm, 6 nm, and 11 nm, respectively. E) The Si EDS map corresponding to Figure 5D is shown, highlighting three stacked Si dots. F) A higher magnification of the top Si dot in Figure 5D is shown, with the Ge-rich shell surrounding the Si dot highlighted by black arrows. G) The middle dot of the pillar in 5D with a corresponding graphic shown in H) demonstrates the 3-D layers present in the nanostructure. The oxide has been removed from the Si/SiGe pillars before imaging for increased resolution.

To investigate the composition of the oxidized pillars, EDS, and electron energy loss spectroscopy (EELS) analysis were used to reveal Ge concentrations up to 80% in the SiGe after oxidation (compared to the initial 30% Ge concentration). Our nanostructures remain dislocation-free despite the lattice mismatch between Si and $Si_{0.2}Ge_{0.8}$ *[16]*. A possible explanation is that some strain relaxation has occurred through elastic deformation due to high free surface area of the nanowires *[17]*, rather than plastic deformation as would be evidenced by dislocations.

4.3. Investigation of Ge Shell around Si QD

Interestingly, a bright halo in the HAADF STEM images suggesting higher Ge content around the encapsulated Si QD is observed during longer oxidation times as indicated by black arrows in Figure 5F and the illustration in Figure 5H. Other sources besides compositional differences can also cause intensity variation in STEM imaging of crystalline materials, including strain fields and sample thickness variations. HAADF STEM simulations were carried out using SICSTEM software *[18]* and compared to experimental HAADF STEM images. A good agreement between the experimental and Ge-shell simulation data suggests that a Ge-rich shell, and not strain, is the cause of the change in intensity for the experimental STEM image.

We also carried out molecular dynamics (MD) and density functional (DFT) calculations to investigate the thermodynamic favorability of Ge shell formation around an encapsulated Si dot. The results are summarized in Figure 6. From MD calculations, we retrieve an overall energy difference of 10 meV/atom between the Ge shell and no Ge shell structure, favoring the formation of a Ge shell. However, this result should be treated with caution as the energy difference is below the size of typical systematic errors in MD simulations. Further, the interatomic potentials in our MD calculations do not explicitly treat the electronic structure of the chemical bonds comprising the interface. Therefore, we use DFT to make an energetic comparison based on a fully quantum mechanical approach to the electronic structure. Applying DFT to slices of the atomic configurations realized in the MD simulation, we predict a total free energy difference of approximately 50 meV/atom in favor of Ge shell formation. While this energy difference is still within the methodological uncertainty of DFT, multiple chemical tools parameterized at both a classical and quantum mechanical level indicate that Ge shell formation is, in fact, a thermodynamically favored outcome for these Si QDs.

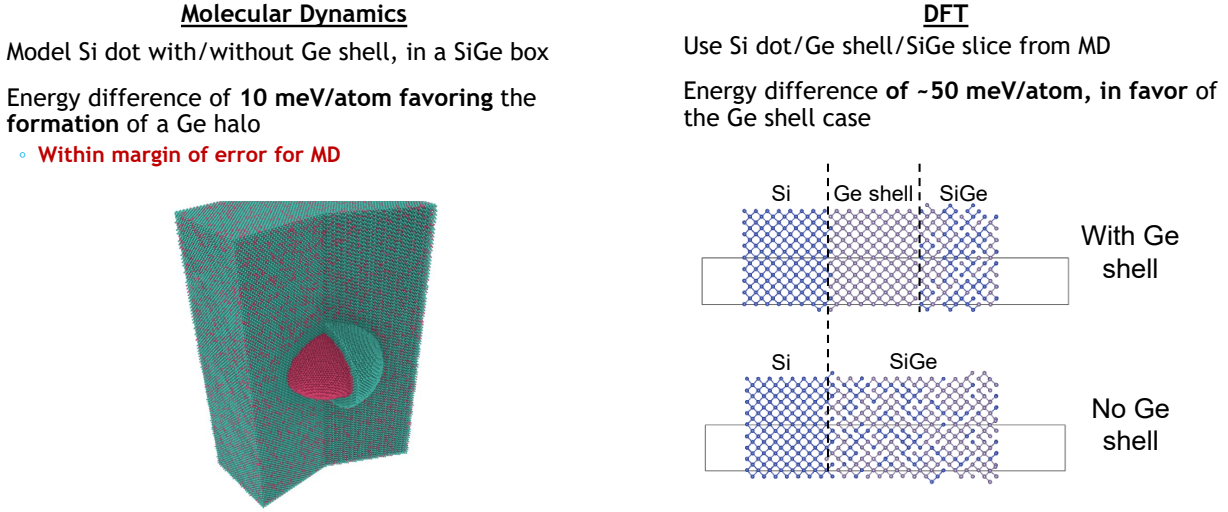

Figure 6. Summary results of theoretical calculations for the formation energy of Si QDs with and without the Ge shell.

4.4. Strain And Electronic Structure Of Si QDs

The strain present in the Si QD and surrounding material will affect the band structure and band alignment present in these nanostructures, which will in turn affect the utility of these QDs for

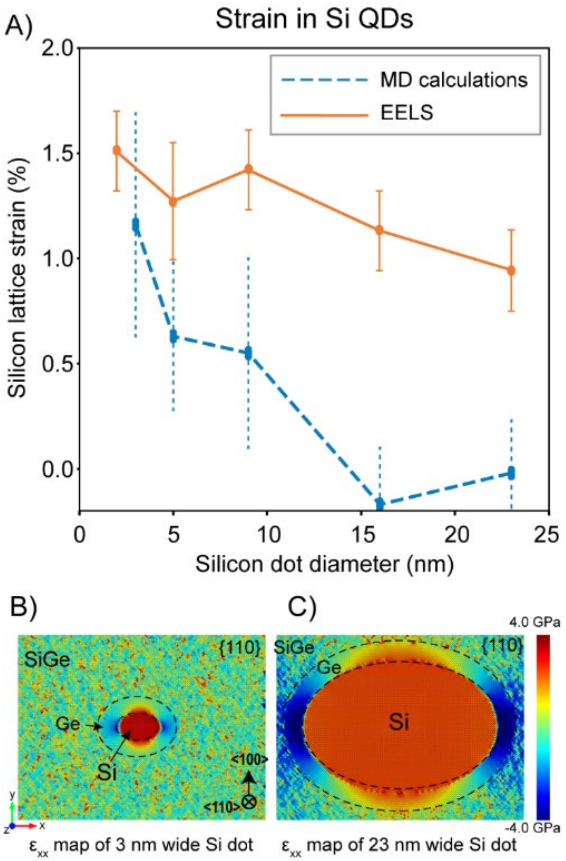

Figure 7. Strain calculations for a range of Si dot sizes using molecular dynamics (MD) and electron energy loss spectroscopy (EELS). A) MD simulations (blue dashed line) and strain calculated from EELS (orange line) show a trend for higher strain as the dot diameter decreases. Computational stress maps for B) a 3 nm wide Si dot and C) a 23 nm wide Si dot reveal higher levels of stress in the smaller Si dot and a fairly even distribution of stress within each QD.

device applications. Conventional experimental methods to determine strain from atomic resolution STEM images using geometric phase analysis are frustrated by the embedded nature of the Si QD. To address this, strain values were extracted from the MD calculations, as shown in Figure 7. Stress on the silicon is hydrostatic and tensile while stress on the Ge shell is non-uniform and compressive. Figure 7A shows the inverse relationship between strain of the Si QDs and QD diameter. Error bars account for variations in strain across the Si QDs. Computational stress maps, as seen in Figure 7B and 7C, reveal that the vast majority of stress on the system is placed on the Si dot and surrounding Ge shell with stress in the surrounding SiGe rapidly approaching zero. As the ratio of the Si dot to SiGe pillar diameter becomes larger, the Si lattice parameters appear to dominate, leading to roughly zero lattice strain in the Si for the 16 nm and 23 nm diameter Si dots.

The electronic structure of our strained Si QDs differs significantly from bulk Si due to the presence of both strain and quantum confinement. To investigate this, monochromated EELS inside a 60 kV STEM was used to measure high-resolution Si $L_{2,3}$ edges for the embedded Si QDs. The near-edge fine structure in these spectra, shown in Figure 8, is a direct measure of the unoccupied conduction band (CB) density of states *[19]*. Figure 8A shows the spin-3/2 component of the $L_{2,3}$ spectra after background removal of the portion of the Si/SiGe nanostructure with only SiGe and the portion of the Si/SiGe nanostructure with the embedded Si dot/Ge shell. Figure 8B is the $L_{2,3}$ spectra of just the Si dots, a result of subtracting the SiGe pillar/Ge shell contribution from the Si dot/Ge shell/SiGe pillar spectra. The inflection points, indicated by red markers, give the energy of the conduction band minima (CBM) *[20]*. We see a large difference of approximately 350 meV in onset energy between the $Si_{0.2}Ge_{0.8}$ pillar and Si substrate spectra, suggesting a type-II band alignment that would allow charge trapping on the Si QDs. We see that the near-edge structures of the Si QDs resemble that of bulk unstrained Si, suggesting that our QDs are under hydrostatic strain and no splitting of CB valleys has occurred *[20]*.

The Si QD energy shift consists of three contributions as illustrated in Figure 9 a strain-dependent shift in the 2p core levels, a strain-dependent shift in the Si Δ valleys, and a shift due to quantum confinement for electrons occupying the Si QDs under a type-II band alignment. The

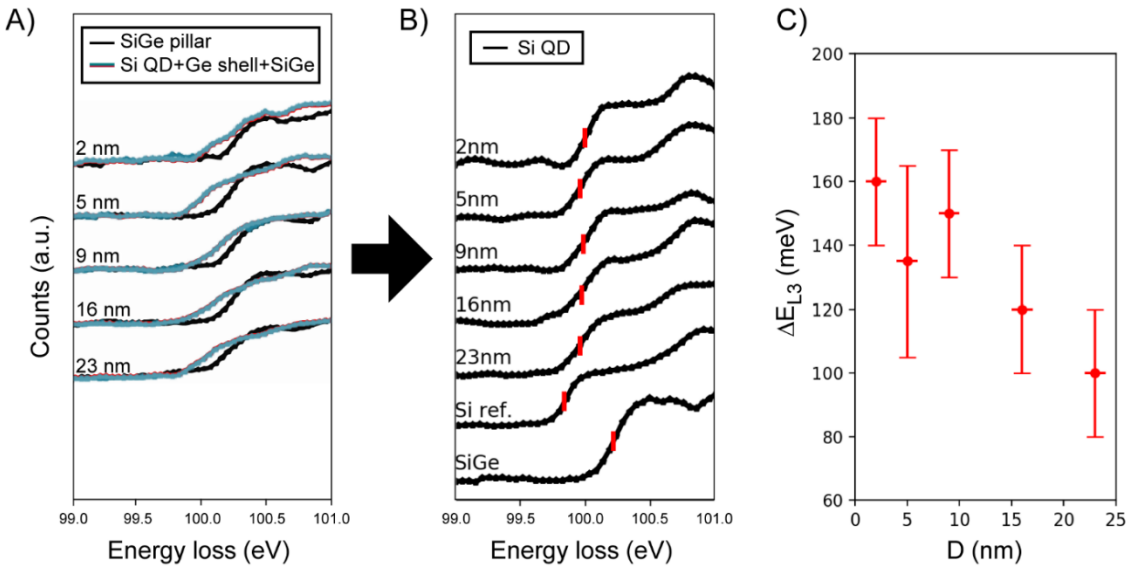

Figure 8. EELS data for a range of Si QD diameters encapsulated in SiGe pillars. A) Conduction band DOS for the SiGe pillar and for the Si QD/Ge shell/SiGe pillar nanostructure for varying sizes of Si QD diameters. B) Conduction band DOS for Si QDs with varying sizes are shown, with bulk unstrained Si (Si ref.) and Si0.2Ge0.8 (SiGe) as labeled. The red markers highlight the inflection point of each edge onset. C) The change in energy of the Si L3 edge onset is shown as a function of Si QD diameter (D).

two strain-dependent shifts push the respective energy levels in opposite directions, increasing the relevant transition energy under hydrostatic tensile strain. The effect of confinement also tends to increase the relevant transition energy and only implicitly depends on strain in that the relevant band offsets depend on strain.

To compare with the MD calculations, we estimate the magnitude of the strain in our Si QDs using EELS data. By employing the equation shown in Figure 9, with an estimated 2p core level shift of 6 eV *[21]* and the aggregate shift in the Si Δ CBM due to the dilatation and uniaxial deformation potentials inferred as 4.6 eV *[22]*, we expect that a 1% hydrostatic tensile strain will result in a 106 meV shift in the transition energy probed by EELS relative to bulk Si. If we neglect the effect of quantum confinement, the strain in our Si QDs calculated using EELS data is shown in Figure 7A. While this estimate of the strain is fairly consistent with the MD calculations for the smaller dots, the strain in the larger dots significantly deviates from the MD calculations. While quantum confinement may play a role in shifting the Si QD $L_{2,3}$ spectra, a lack of direct constraints on the electronic structure of the Ge-rich shell around the Si QDs makes calculating this effect difficult.

To understand the band alignments of the Si QD, Ge shell, and SiGe pillar, we first turn to our EELS measurements, which indicate that the conduction band offset (CBO) between the Si QD and the surrounding SiGe is at least 200 meV. However, we do not know what the relevant offset is between the Si dot and the Ge shell. Further, the inhomogeneous nature of the strain in the Ge shell predicted by our classical MD calculations suggests that the band offset and the valley structure of the relevant conduction band minima in the Ge shell might be highly non-uniform. To estimate how large the Si dot/Ge shell band offset might be, we employ a simple effective

mass model in which each region is characterized by a constant potential and the effective mass of a single bulk-like valley (Δ in the Si QD, L in the Ge shell). We fix the CBO between Si and SiGe to 200 meV and allow the offset between Si and Ge to vary to rationalize the observed

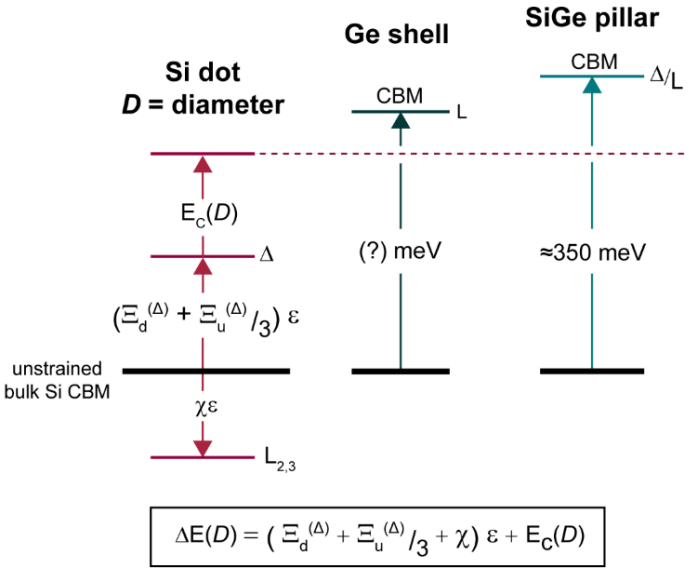

Figure 9. The conduction band minimum (CBM) offsets for the Si dot, Ge shell, and SiGe pillar. The shift in the D valleys of the Si dot due to hydrostatic strain is given by the product of the strain and a particular combination of the dilatation ($\Xi_d^{(\Delta)}$) and uniaxial ($\Xi_u^{(\Delta)}$) deformation potentials. The total shift in the energies of bound states in the Si dot is then given by the sum of this strain-dependent shift in the D valleys, the shift in core-level energies due to strain ($\chi\varepsilon$), and the shift due to quantum confinement ($E_C(D)$). Relative offsets from bulk Si for the Ge shell (unknown) and the $Si_{0.2}Ge_{0.8}$ pillar (≈350 meV) are illustrated.

EELS shift and the strains predicted by classical MD. For the 2 nm and 5 nm Si QDs, we predict the Ge shell would need to be offset 150 meV below and 5 meV below the Si QD, respectively, in order to bind an electron to the QD.

Using this model, we are able to tentatively estimate the strain at approximately 1% for all of our QDs, but further analysis is needed to sharpen our understanding of this system. The strain-dependent 2p core level shift, the CBO between the Si core and Ge shell, and the inhomogeneous nature of the strain in the shell all need to be more precisely constrained. Atomistic tight-binding calculations may be a promising modeling tool to resolve ambiguities in our analysis and to help better understand both the EELS and the opportunities for optoelectronic applications in this novel system.

5. ELUCIATING THE ENHANCED GE DIFFUSION MECHANISM DURING THERMAL OXIDATION OF SI/SIGE NANOWIRE-FIN STRUCTURES

In this section, we describe the experiments carried out as well as the density functional theory (DFT) calculations that are in progress to elucidate the mechanism of the observed enhanced Ge diffusion mechanism during high temperature thermal oxidation.

5.1. Motivation

Brewer et al. recently reported a novel Ge diffusion process that resulted in vertically stacked, strained, Si nanowires encapsulated in SiGe during high temperature oxidation of a multilayered Si/SiGe nanofin *[1]*. There are a few fundamental processes that occur during the oxidation-induced formation of these embedded Si nanowires, of which two are well studied. First, there is the interdiffusion of Si and Ge from the alternating Si/SiGe layers. This interdiffusion is sufficiently slow for the layers to not impact the formation of the nanowires*[23-28]*. Additionally, during the oxidation of SiGe, there is a selective oxidation of Si to form SiO_2 rather than GeO_2, which results in a pile-up or snow-plow effect with an enhanced Ge concentration in the SiGe layer near the SiGe/SiO_2 interface *[29-32]*. Brewer et al. reported that in the Si/SiGe fin structure there is an additional, rapid movement of Ge down the oxidizing sidewall, which was previously unreported. This movement ultimately causes the encapsulation of the Si layers and leads to the formation of defect-free, single crystal Si nanowires embedded in SiGe nanofins. The size of the nanowires was controllable down to ~2nm in diameter by increasing oxidation time. The number of wires formed depends on the number of Si/SiGe layers that are grown. While this offers an exciting potential pathway to next generation microelectronic structures and other device applications, little is known about the exact mechanism behind this unique, rapid lateral diffusion of Ge down the sidewalls of Si/SiGe fins.

This study aims to further investigate the novel, rapid lateral diffusion of Ge during the high temperature oxidation of a multilayered Si/SiGe fin to elucidate the mechanism for this tremendous enhancement in diffusivity.

5.2. Activation Energy Extractions

The initial fin structure is shown in the cross-sectional STEM image in Figure 10 (a) and at higher magnification in Figure 10 (b). Samples were annealed with dry O_2 flowing for a series of times between 750-900°C. After high temperature oxidation, there is movement of Ge down the oxidizing Si interface. The diffusion of Ge down the side, shown in Figure 10 (c) and (d), forms a triangular shape with a thicker amount of laterally diffused Ge near the Si/SiGe interface. The initial steps of the Ge movement are captured and measured as a lateral diffusion length, as labeled in Figure 10 (d). Figure 10 (e) shows the defect-free interface between the laterally diffused Ge and the Si layer.

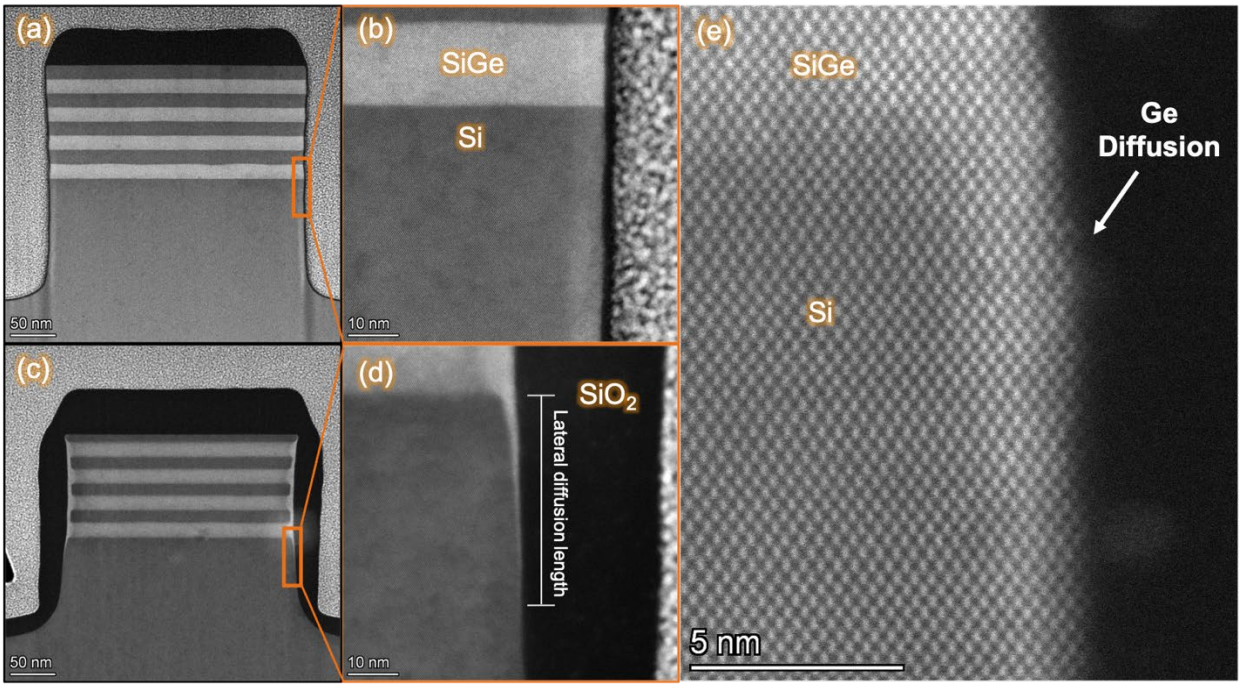

Figure 10. (a) cross-sectional STEM image of a multilayered Si/SiGe fin before oxidation and (b) is a zoomed in STEM image of the same fin, showing that there is no Ge lateral diffusion. (c) is a cross-sectional STEM image of a fin after 20 minutes of dry oxidation at 900°C. (d) is a zoomed in STEM image of the same oxidized fin, showing that Ge diffuses down the oxidizing interface. (e) is a lattice STEM image showing the defect-free interface between base Si layer and the laterally diffused Ge.

To study the rate of lateral diffusion down the Si/SiO_2 interface, the lateral diffusion length was measured through the analysis of HAADF-STEM images as defined in Figure 10 (d). A minimum of three different times was studied for each annealing temperature. The annealing times were adjusted at each temperature based on the oxidation rate. The goal was to keep the thickness of the grown oxide (16 to 34nm) roughly the same for each temperature set.

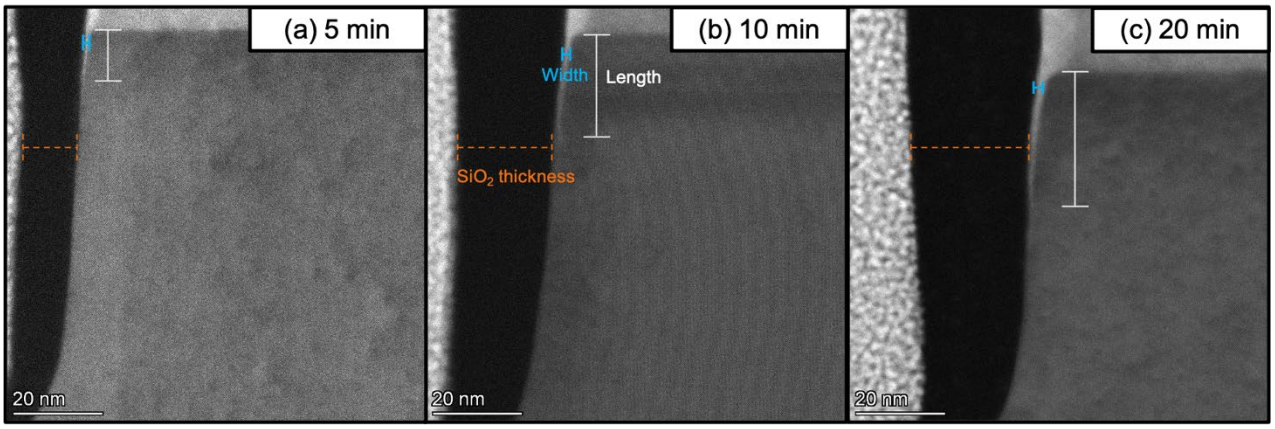

Figure 11. cross-sectional STEM image of the Si/SiGe fin after oxidation at 900°C for (a) 5 mins, (b) 10 mins, and (c) 20 mins. The dashed orange line shows the thickness of the thermally grown SiO_2, the blue line indicates the lateral diffusion width, and the solid gray line shows the lateral diffusion length of the Ge.

Figure 11 shows cross-sectional STEM images of three different fins after oxidation at 900°C with increasing oxidation time from (a) to (c). It can be seen that both the diffusion length and width of the Ge increased as oxidation time increased. It was found that the diffusion length and width varied linearly with the square root of time, as shown in Figure 12 (a) and (b), thus suggesting that the diffusion exhibits a simple $\sqrt{Dt}$ dependence. This correlation of the diffusion length and width with the square root of oxidation time allowed for the extraction of a diffusion coefficient at four different temperatures ranging from 750-900°C.

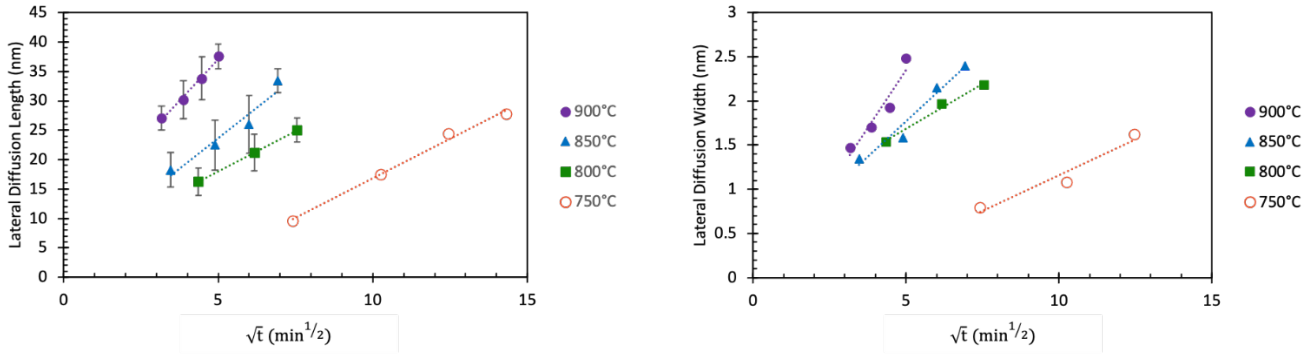

Figure 12. L: a plot showing the linear relationship between lateral diffusion length and the square root of oxidation time. R: a plot showing the linear relationship between lateral diffusion width and the square root of oxidation time.

Figure 13 shows the Arrhenius plot of the data extracted in Figure 12 for the diffusivity as a function of temperature. This plot indicates that the activation energy of Ge diffusion down the oxidizing interface is 1.1±0.3 eV while the activation energy for Ge diffusion into the fin is 1.6 ±0.2 eV (Figure 13). These activation energies are both significantly lower than the 4.8eV activation energy of Ge diffusing into pure Si, resulting in diffusion coefficients a few thousands of times lower than those extracted for the diffusion of Ge down the oxidizing interface *[33]*.

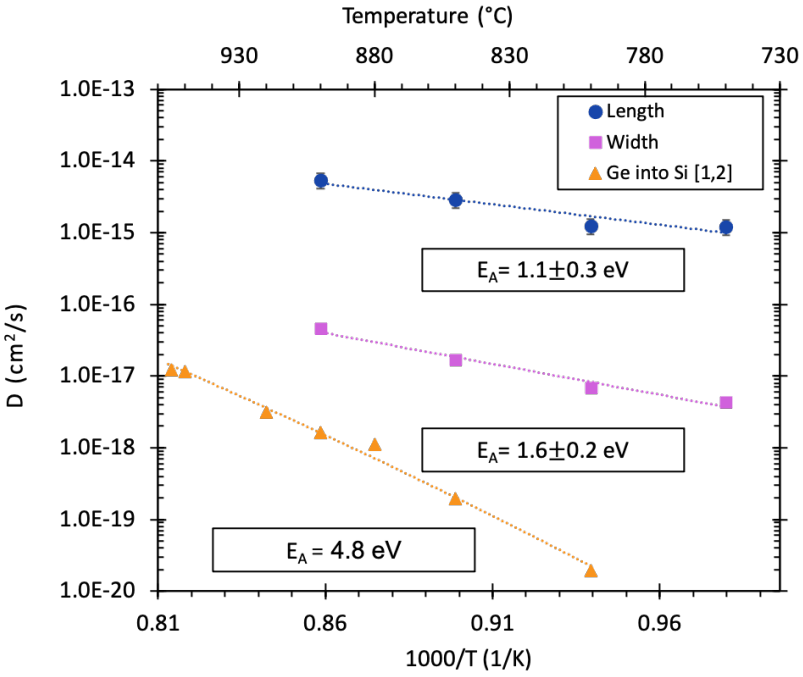

Figure 13. Arrhenius plot of Ge diffusion down the oxidizing interface (length) and into the fin (width) with activation energies of 1.1 and 1.6 eV, respectively. Ge diffusion into Si data taken from *[33, 34]*.

5.3. Proposed Mechanism

The observed lateral diffusion of Ge along the interface is 3-4 orders of magnitude faster than diffusion of Ge into Si and around 2-3 orders of magnitude faster than Ge diffusion into $Si_{0.7}Ge_{0.3}$. This phenomenon cannot simply be explained by an interdiffusion of Si and Ge. The predicted diffusion length of Ge into bulk Si for these times and temperatures is significantly shorter than what is experimentally observed for the lateral diffusion of Ge. As an example, the predicted diffusion length of Ge into bulk Si at 900°C for 20 minutes is only 0.4nm while it is observed that the lateral diffusion length of Ge is 33nm *[33]*. Thus, a standard Ge diffusion mechanism through bulk Si is ruled out. It is well known that interfacial diffusion in some materials systems can be much faster than bulk diffusion *[35]*. This raises the possibility that Ge is moving down the interface due to interfacial diffusion. To test this hypothesis, a sample was encapsulated in a quartz ampule, which was vacuum sealed. The sealed quartz ampule was then annealed at 900°C for 10 minutes. The glass ampule greatly reduced the oxidation of the surface during the high temperature anneal. The amount of grown oxide was reduced from approximately 20nm to around 5nm by using the sealed ampule (Figure 14). Correspondingly, it can be seen in Figure 14 (b) that very little diffusion down the interface is observed, indicating that the lateral diffusion of Ge is not simply an example of rapid interfacial diffusion. Rather, it can be inferred that active oxidation is a requirement for the observed, enhanced lateral Ge diffusion.

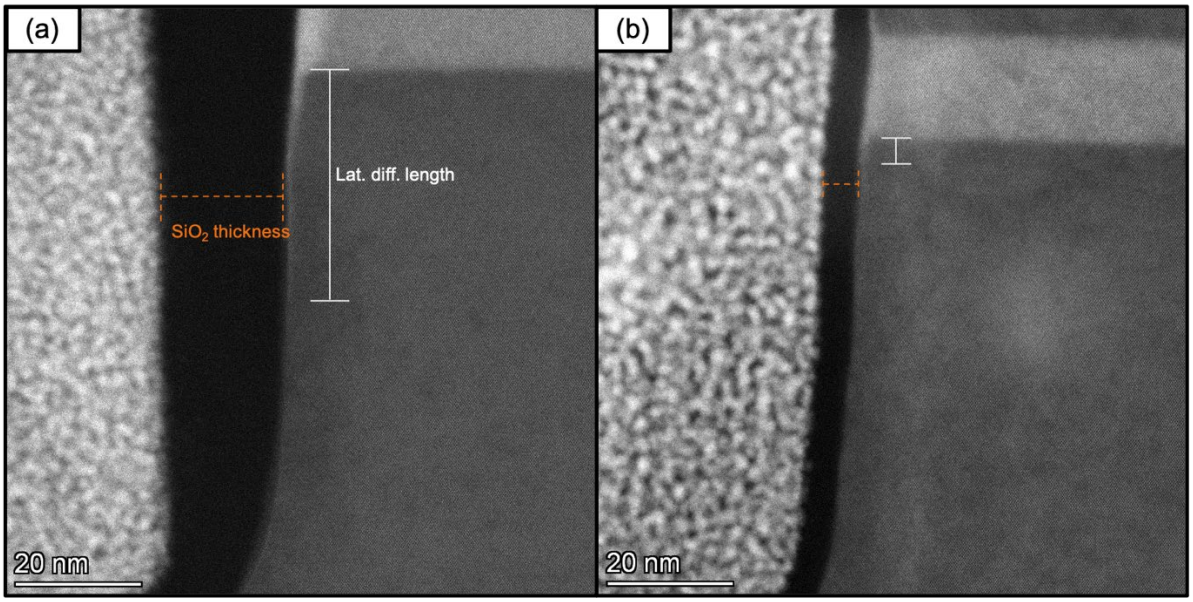

Figure 14. Difference in the lateral diffusion lengths after 10 minutes at 900°C of (a) oxidation in dry O_2 and (b) an anneal under forming gas.

When considering the potential pathways through which the Ge could diffuse there are three primary locations to consider as summarized in Figure 15. The first potential mechanism for the Ge diffusion during active oxidation is within the crystalline Si side along the interface (Figure 15, pathway 1). Another potential pathway is that Ge diffuses through the bulk oxide and is subsequently reintroduced down the interface (Figure 15, pathway 2). However, the diffusivity of Ge into bulk oxide is even slower than Ge diffusion into bulk Si, and diffusion at 900°C for 20 mins would result in just 0.1 nm of movement of Ge into the bulk SiO_2 *[36]*. This suggests that movement of Ge through bulk SiO_2 followed by a reinsertion into the Si fin is highly unlikely.

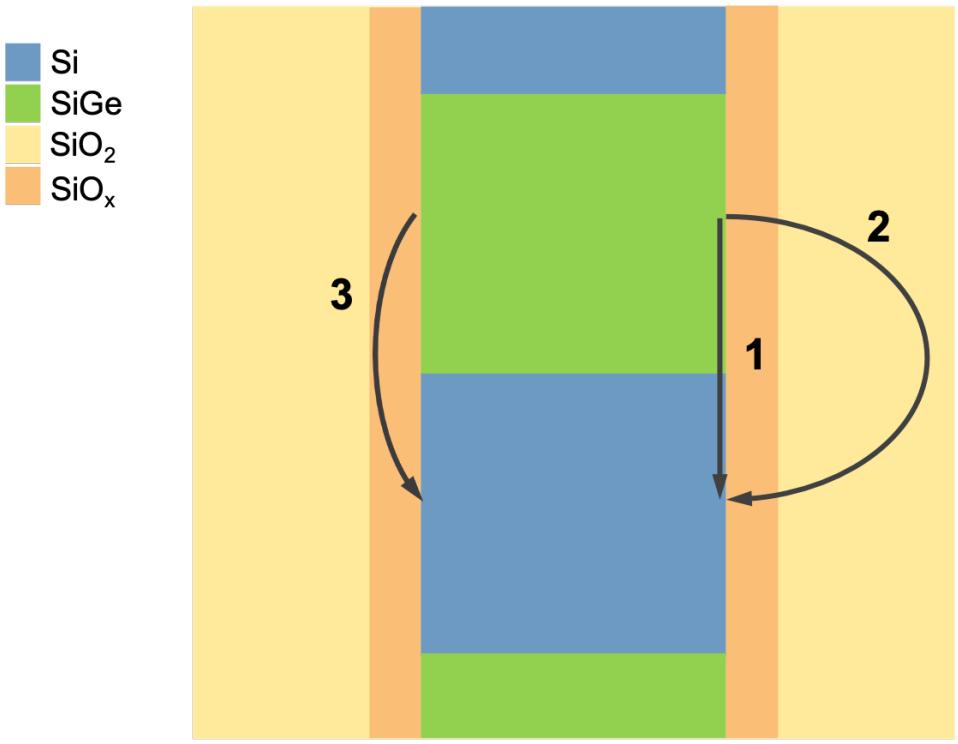

Figure 15. Potential mechanisms for Ge diffusion (1) through the fin material, (2) through the bulk oxide, and (3) through the suboxide

The final potential pathway is diffusion of the Ge through the suboxide followed by a reinsertion process (Figure 15, pathway 3). The suboxide is a transition layer between crystalline Si/SiGe and the amorphous, stoichiometric SiO_2layer at the interface that is typically around 1 nm thick and is characterized by an abundance of oxygen vacancies. It has been reported that the number of defects in this region could be as much as 4 orders of magnitude higher than in bulk SiO_2 *[37]*. This transition region could provide an enhanced pathway for the experimentally observed rapid Ge diffusion along the Si/SiO_2 interface. Previous work from Rashkeev et al. has indicated that H^+ diffuses differently along the Si/SiO_2 interface depending upon the suboxide character at the interface *[38]*. Because there is not a unified opinion on whether Ge is more stable in the suboxide or on the crystalline side of the interface during oxidation, Ge diffusion on the crystalline and suboxide sides of the interface must be considered *[39-43]*. We postulate that Ge diffusion occurs either in the suboxide, followed by a reinsertion into the Si fin or down the Si side of the interface through some active exchange process facilitated by active oxidation (Figure 15, pathway 3 or pathway 1).

To determine which of these two pathways is more likely, an experiment was conducted in which a sample was oxidized for 24 minutes at 850°C. The sample was the etched in HF for 90s to remove the thermally grown oxide and was then oxidized for an additional 24 minutes at 850°C. This sample could then be compared with ones that had been oxidized for 24 and 48 minutes without the HF etch. This experiment is summarized in Figure 16.

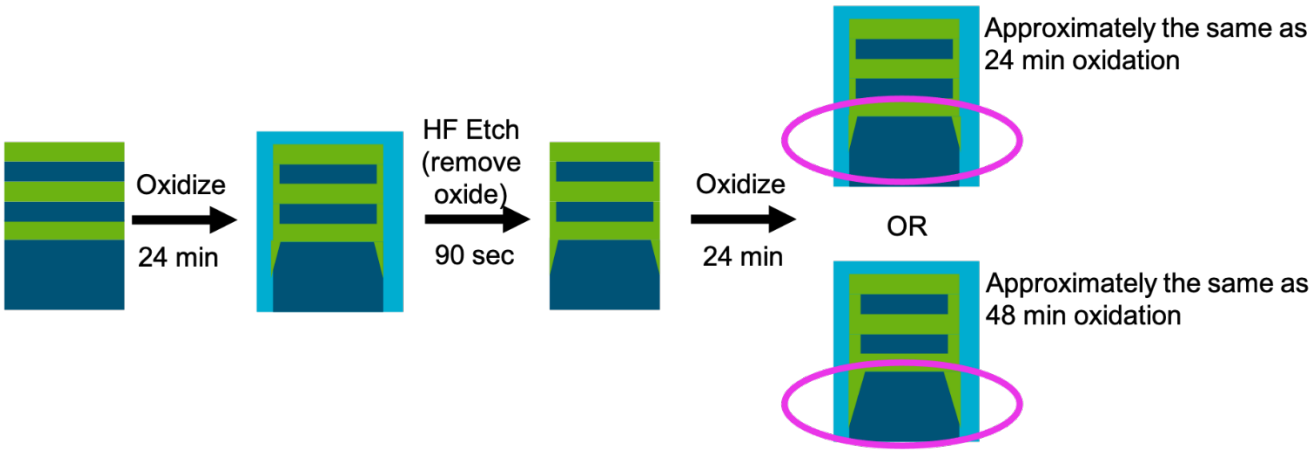

Figure 16. Schematic of experiment carried out to determine whether Ge diffusion occurred through the suboxide or the crystalline side of the interface

The goal of this experiment was to determine whether the thermally grown oxide was acting as the source of Ge that was moving down the interface. This information could be inferred by comparing the lateral diffusion length of the triangular finger between the etched and un-etched samples.

Figure 17 shows the results of this experiment. The 24 min oxidation and the etched sample have approximately the same lateral diffusion length.

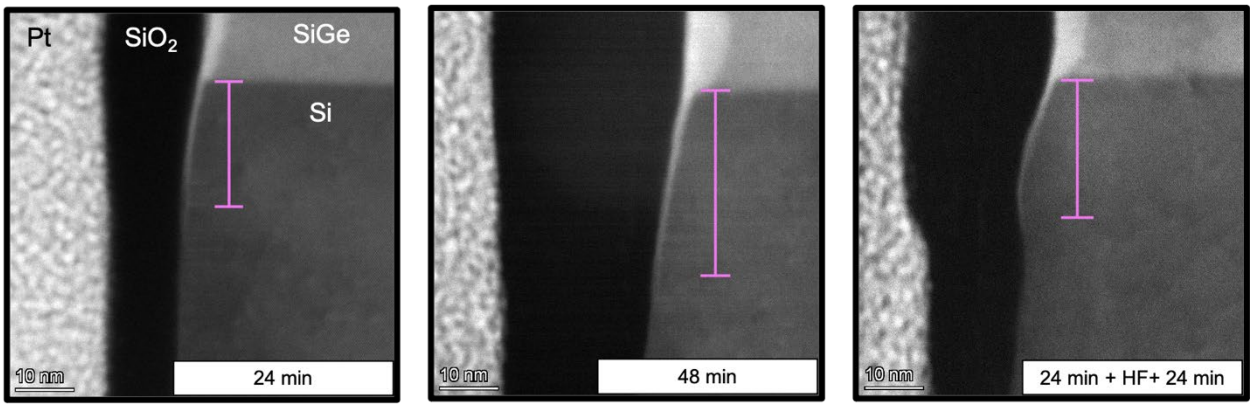

Figure 17. STEM images of fins that have been oxidized at 850°C for (a) 24 mins, (b) 48 mins, and (c) 24 mins with a 90s HF etch followed by 24 more mins.

This result indicates that when the oxide is removed, the lateral diffusion is stalled. Because of this, it can be postulated that the Ge moves predominately through the suboxide (Figure 16, pathway 3). These results will seek to be supported through DFT calculations to gain additional insight into the preferred pathway through the suboxide and the rate-limiting step of the overall diffusion mechanism.

6. A HYPOTHESIS FOR RAPID DIFFUSION NEAR INTERFACE AS (2+)

The experimental diffusivity of Ge in bulk Si, in bulk SiGe, and in bulk SiO_2 is observed to be much slower than would be needed to explain the fast lateral diffusion of Ge along the Si/a-SiO_2 interface. As an initial iso-chemical proxy for Ge, Yu and Hwang had performed DFT calculations for the structure and diffusion of excess Si atom in SiO_2, both in crystalline quartz and in a model of amorphous silica *[44]*. The neutral silicon atom was found to diffuse with large migration barriers, 2-3 eV in quartz increasing to 4.5-5 eV in silica, that latter in good agreement with estimates from experiment that indicate slow diffusion. Extended the analysis to Ge, Yu and Hwang found diffusion barriers of 1.7 eV in quartz increasing to 2.5 eV in silica. In calculations at SiO_2/Si interfaces found that the Ge interstitial would undergo thermally activated site exchange to kick out a lattice Si atom which would then incorporate into the SiO_2 layer near the interface. The segregation of the Ge into the Si was proposed to be the process for the formation of Ge nanoparticles in an Si-rich oxide matrix. This then provides a mechanism for incorporation of Ge into the Si at the interface, but the question then was the mechanism of transport down the interface to an incorporation site.

The hypothesis we explore in this section was inspired by the unexpected computational result from 2004 *[45]* that a neutral hydrogen approaching a Si-SiO_2 interface from deep in the silica would spontaneously ionize as it approached the interface. As a neutral atom, the hydrogen would diffuse rapidly (with low migration barriers) through bulk silica, and the ionization level was too deep in the gap to form a proton, which would bond to a bridging oxygen and become immobile. Near the interface, however, the H atom would spontaneously bond to an oxygen, indicating the loss of an electron, ionize to the silicon conduction band and the charged proton further stabilized by the Coulombically localized electron in the conduction band of the nearby silicon.

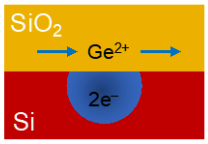

Figure 18 – Model for fast diffusion near interface

A plausible hypothesis is illustrated in Figure 18. A Si or Ge interstitial near the interface could similarly become ionized to a Coulombically localized conduction band in the silicon. The cause of the slow diffusion of the neutral species in bulk is the tendency of the neutral atom to bond into the network to eliminate the dangling orbitals on the atom, and the barrier to migration therefore involves the breaking and making of bonds and being on the scale of a bond energy. In bulk semiconductors (e.g. GaAs and Si), it has been observed that ionized species diffuse much more rapidly, even athermally, as positive ions, where the ionized species diffuses primarily through interstices in the lattice, without bonding in the network, needing to overcome steric barriers rather than a bond energy to be transported through the lattice. The hypothesis we test here is: if ionized to their s^2 (2+) valence state SiO_2, the Si and Ge would similarly diffuse with much lower barriers.

6.1. Computational Methods

The density functional theory calculations are executed with Sandia's SEQQUEST code. The calculations use the Perdew-Burke Ernzerhof (PBE) flavor of the generalized gradient approximation [GGA-PBE]. A generalized norm-conserving pseudopotential of the Hamann form [GNCPP] was used for the Si atom, the "hard" pseudopotential for the O atom was generated within the Troullier-Martins form [TMPP]. The atomic basis sets were contracted Gaussian functions of "double-zeta plus polarization" (DZP) quality. Preliminary defect calculations used hexagonal 2x2x2 (72-atom) supercells with a 2x2x2 *k*-point mesh, and the production results used 3x3x3 (243 atom) supercells of the conventional a-quartz lattice with just the G-point to sample the Brillioun Zone, the larger cell being necessary to better capture the long-range elastic effects of an interstitial in the network structure. The atoms are allowed to fully relax to their equilibrium positions, until all forces on the atoms were less than 0.015 Ry/Bohr, sufficient to converge the equilibrium energy to less than 0.01 eV.

The charged defect calculations in supercells used the local moment countercharge (LMCC) to impose the correct boundary conditions for a localized charge in a supercell calculation *[46, 47]*. This approach has been demonstrated previously to successfully analyze the energetics of the structure and electronic properties of oxygen-deficient defects in silica, including ionized charge states *[48, 49]*, additional validation evidence for the current study.

6.2. The Perfect Crystal

As a preliminary model for interstitial diffusion, a perfect crystal is used instead of an amorphous silica model. There is no single diffusion path within an amorphous silica, one would need to do a statistical analysis of a large number of possible paths—impractical and unnecessary for this model assessment. The a-quartz is often used as a proxy for calculations of defects in silica, but a cristobalite model would provide a better match to the density of silica, and might be the more representative model. Calculations to optimize the quartz and cristobalite crystal structures within PBE were performed, and revealed an inconvenient sub-polymorphism, where multiple minima could be obtained within each polymorph, separated by very small energy differences, differentiated by discrete differences in the twist-tile orientation of the constituent SiO_4 polyhedra. This complicated the determination of an optimum structure, and foreshadowed challenges in determining ground state relaxed defect structures stemming from the easy coordinated re-orientation of these polyhedral. Plans to use the more representative cristobalite structure were abandoned, because its sub-polymorphism was more complicated, and because the pre-existing literature for defects in quartz provided some benchmark results. The computed lattice parameters we obtain for the PBE quartz were a0=5.027Å and c0=5.526Å, in reasonable agreement with previous literature and with experiment. These lattice parameters were used in the supercell calculations of defects, and were held fixed (while all the atoms with the supercell relaxed).

6.3. Neutral Silicon Diffusion

A first set of calculations to compute the diffusion paths and associated barriers for the diffusion of a neutral silicon interstitial in quartz. Even though the quartz is a crystalline material, the migration paths are exceedingly complicated, navigating between two different bridge sites (the interstitial bridging between a network Si and an oxygen within a Si-O-Si network bond (BC-I and BC-II), and also between two different four-fold structures (FC-I FC-II) sitting within the

interstices in the lattice but attaching to two silicon atoms in the network in distinct Si-Si bonds *[44]*. While differing in many details, our results confirm the essential features obtained by Yu *et al. [44]* – a complex potential energy landscape with multiple minima, with large >2 eV barriers to migrate between the different sites in the lattice.

6.4. Migration of the (2+) Silicon Interstitial

We performed a comprehensive search for equilibrium structure for the $Si_i(2+)$ interstitial, and migration paths that would lead to net transport through the quartz. The search included all the neutral interstitial structures as starting points for a structural relaxation, and added a sampling of the non-bonded interstitial structures that were anticipated to be favored by the (2+), along with a sampling of puckered in-network structures inspired by the puckering observed for O vacancy E' centers that are positively charged.

None of the neutral defect structures proved to be stable in the ion. The energy surface for the $Si_i(2+)$ proved to be much simpler, and exhibit only two distinct important minima, as illustrated in Figure 19:

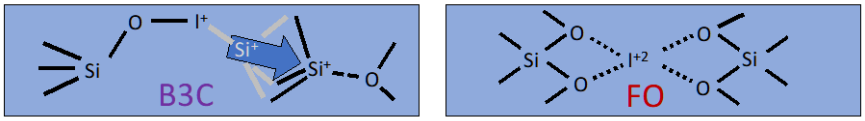

Figure 19 - Stable Si(2+) interstitial defect structures

The first stable structure begins with the neutral bond-bridging structure, except that the network Si retreats to form a back-bond to the a further network oxygen, in direct analogy to the puckering seen in the O vacancy (1+) center. This provides an energy lowering as the Si^+ network atom attaches to the negatively charge O network atom, while the interstitial I^+ remains attached to the bridging oxygen. This structure, labeled "B3C", is the lowest energy configuration we found.

A second stable structure was in a non-network site, where the I^{2+} sits in an interstitial site weakly coordinated with four oxygen atoms, a site labelled "FO". The net positive charge on the I is stabilized by the slightly negative oxygen atoms in the network. To attain this configuration around the defect required significant and long-range reorientation of the network around the I^{2+} in order to coordinate all four oxygen atoms to the interstitial. This is possible because of the low energy to tilt-twist the SiO_4 tetrahedra, already foreshadowed above in the description of the perfect crystal. What complicated this search is that this reorientation involved the coordinated twist/tile of for a large number of tetrahedra. This structure was found to be only 0.5 eV above the ground state B3C structure, auguring well for a relatively flat potential energy surface that would be amenable to low-energy diffusion.

Within the non-network interstices of the network, the migration path of an FO site to another FO site was discovered that led to a migration barrier of only 0.1 eV. The weak coordination to the network oxygen enables shuttling of the non-bonded interstitial through the interstices, without requiring a breaking of a covalent bond, and only requiring the low-energy tile-twist reorientation of the surrounding lattice to shuttle the interstitial from one site to the next. The barrier for the interstitial to be trapped into the lower energy network site is 0.3 eV, higher than

the energy required to migrate through the lattice, and also requiring a significant local recoordination. Once the interstitial enters the interstices, it migrates very quickly through the lattice.

The overall activation for diffusion is dictated by the emergence of the interstitial from the in-network B3C site, which in these calculations is determined to be limited by a 0.8 eV energy barrier. The overall process is illustrated in Figure 20.

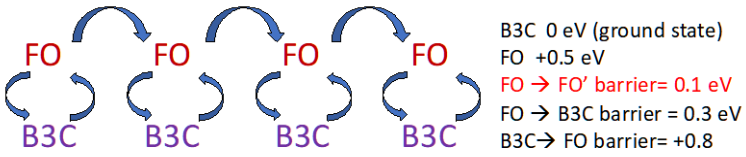

Figure 20. Migration path of the I(2+)

The overall activation energy of the Si(2+) is then <1 eV, where the barrier is dictated by the exit of the Si interstitial from its in-network B3C site into the non-network interstitial sites, which then leads to rapid diffusion of the Si(2+) through the channels in the lattice. This barrier is significantly lower than the 2-3 eV barriers observed for the migration of the neutral Si, and would be facilitate rapid diffusion at low temperatures.

6.5. Summary

The goal of this section was to propose and test a hypothesis that would enable the fast diffusion of the Ge interstitial at or near the Si/SiO_2 interface. The results for the Si(2+), iso-valent with the Ge, indicate that the a (2+) species indeed will diffuse with much lower barriers than the neutral defect. The neutral defect inserts itself into the network lattice and requires bond energies in order to diffuse. The (2+) defect does not need to bond its missing *p*-electrons, and finds it much more favorable to sit in non-bonded interstitial, through which it is easier to defuse, limited by low-energy lattice reorientation energies rather than bond energies. While the analogous Ge calculations were not fully completed, it is expected that a similar salutary process would be operative, even more so. The Ge oxide is less favorable than the Si oxide, suggesting that the in-network bonding site such as the B3C would be less stable, and that the Ge would find much faster migration as the (2+).

REFERENCES

[1] W. M. Brewer, Y. Xin, C. Hatem, D. Diercks, V. Q. Truong, K. S. Jones, "Lateral Ge Diffusion During Oxidation of Si/SiGe Fins", *Nano Letters*, ***17***, 2159 **(2017)**.

[2] M. O. Baykan, S. E. Thompson, T. Nishida, "Strain effects on three-dimensional, two-dimensional, and one-dimensional silicon logic devices: Predicting the future of strained silicon", *Journal of Applied Physics*, ***108***, 093716 **(2010)**.

[3] E. M. Turner, K. R. Sapkota, C. Hatem, P. Lu, G. T. Wang, K. S. Jones, "Wet-chemical etching of FIB lift-out TEM lamellae for damage-free analysis of 3-D nanostructures", *Ultramicroscopy*, ***216***, 113049 **(2020)**.

[4] J. Mayer, L. A. Giannuzzi, T. Kamino, J. Michael, "TEM Sample Preparation and FIB-Induced Damage", *MRS Bulletin*, ***32***, 400 **(2007)**.

[5] D. J. Lockwood, X. Wu, J. M. Baribeau, S. A. Mala, X. Wang, L. Tsybeskov, "Si/SiGe Heterointerfaces in One-, Two-, and Three-Dimensional Nanostructures: Their Effect on SiGe Light Emission", *Frontiers in Materials*, ***3***, 1 **(2016)**.

[6] D. K. Nayak, N. Usami, S. Fukatsu, Y. Shiraki, "Band-edge photoluminescence of SiGe/strained-Si/SiGe type-II quantum wells on Si(100)", *Applied Physics Letters*, ***63***, 3509 **(1993)**.

[7] S. Srinivasan, G. Klimeck, L. P. Rokhinson, "Valley splitting in Si quantum dots embedded in SiGe", *Applied Physics Letters*, ***93***, 112102 **(2008)**.

[8] T. David, K. Liu, A. Ronda, L. Favre, M. Abbarchi, M. Gailhanou, P. Gentile, D. Buttard, V. Calvo, M. Amato, J. N. Aqua, I. Berbezier, "Tailoring Strain and Morphology of Core-Shell SiGe Nanowires by Low-Temperature Ge Condensation", *Nano Letters*, ***17***, 7299 **(2017)**.

[9] D. E. L. Oliveira, E. L. Albuquerque, D. J. S. Sousa, G. A. Farias, F. M. Peeters, "Configuration-Interaction Excitonic Absorption in Small Si/Ge and Ge/Si Core/Shell Nanocrystals", *Journal of Physical Chemistry C*, ***116***, 4399 **(2012)**.

[10] L. J. Lauhon, M. S. Gudiksen, D. Wang, C. M. Lieber, "Epitaxial core – shell and core – multishell nanowire heterostructures", *Nature*, ***420***, 57 **(2002)**.

[11] E. M. Turner, Q. Campbell, J. Pizarro, H. Yang, K. R. Sapkota, P. Lu, A. D. Baczewski, G. T. Wang, K. S. Jones, "Controlled Formation of Stacked Si Quantum Dots in Vertical SiGe Nanowires", *Nano Letters*, ***submitted***, **(2021)**.

[12] S. Ye, T. Endoh, "Edge effect in the oxidation of three-dimensional nano-structured silicon", *Materials Science in Semiconductor Processing*, ***93***, 266 **(2019)**.

[13] S. Ye, K. Yamabe, T. Endoh, "Low-density oxide grown thermally on sidewall of Si nanopillars", *Materials Letters*, ***258***, 126780 **(2020)**.

[14] H. Cui, C. X. Wang, G. W. Yang, "Origin of self-limiting oxidation of Si nanowires", *Nano Letters*, ***8***, 2731 **(2008)**.

[15] S. Ye, K. Yamabe, T. Endoh, "Variance Reduction during the Fabrication of Sub-20 nm Si Cylindrical Nanopillars for Vertical Gate-All-Around Metal-Oxide Semiconductor Field-Effect Transistors", *ACS Omega*, ***4***, 21115 **(2019)**.

[16] R. People, J. C. Bean, "Calculation of critical layer thickness versus lattice mismatch for Ge_xSi_{1-x}/Si strained-layer heterostructures", *Applied Physics Letters*, ***47***, 322 **(1985)**.

[17] F. Isa, A. Jung, M. Salvalaglio, Y. A. R. Dasilva, I. Marozau, M. Meduňa, M. Barget, A. Marzegalli, G. Isella, R. Erni, F. Pezzoli, E. Bonera, P. Niedermann, O. Sereda, P. Gröning, F. Montalenti, H. von Känel, "Strain Engineering in Highly Mismatched SiGe/Si Heterostructures", *Materials Science in Semiconductor Processing*, ***70***, 117 **(2017)**.

[18] J. Pizarro, P. L. Galindo, E. Guerrero, A. Yáñez, M. P. Guerrero, A. Rosenauer, D. L. Sales, S. I. Molina, "Simulation of high angle annular dark field scanning transmission electron microscopy images of large nanostructures", *Applied Physics Letters*, ***93***, 153107 **(2008)**.

[19] P. E. Batson, "Silicon L_{2, 3} near-edge fine structure in confined volumes", *Ultramicroscopy*, ***50***, 1 **(1993)**.

[20] C. Euaruksakul, Z. W. Li, F. Zheng, F. J. Himpsel, C. S. Ritz, B. Tanto, D. E. Savage, X. S. Liu, M. G. Lagally, "Influence of strain on the conduction band structure of strained silicon nanomembranes", *Physical Review Letters*, ***101***, 147403 **(2008)**.

[21] J. F. Morar, P. E. Batson, J. Tersoff, "Heterojunction band lineups in Si-Ge alloys using spatially resolved electron-energy-loss-spectroscopy", *Physical Review B*, ***47***, 4107 **(1993)**.

[22] V. M. Fischetti, S. E. Laux, "Band structure, deformation potentials, and carrier mobility in strained Si, Ge, and SiGe alloys", *Journal of Applied Physics*, ***80***, 2234 **(1996)**.

[23] Y. Dong, Y. Lin, S. Li, S. McCoy, G. Xia, "A unified interdiffusivity model and model verification for tensile and relaxed SiGe interdiffusion over the full germanium content range", *Journal of Applied Physics*, ***111***, 044909 **(2012)**.

[24] P. Castrillo, R. Pinacho, M. Jaraiz, J. E. Rubio, "Physical modeling and implementation scheme of native defect diffusion and interdiffusion in SiGe heterostructures for atomistic process simulation", *Journal of Applied Physics*, ***109***, 103502 **(2011)**.

[25] G. Xia, J. L. Hoyt, "Si–Ge interdiffusion under oxidizing conditions in epitaxial SiGe heterostructures with high compressive stress", *Applied Physics Letters*, ***96***, 122107 **(2010)**.

[26] M. Gavelle, E. M. Bazizi, E. Scheid, P. F. Fazzini, F. Cristiano, C. Armand, W. Lerch, S. Paul, Y. Campidelli, A. Halimaoui, "Detailed investigation of Ge–Si interdiffusion in the full range of $Si_{1-x}Ge_x$ ($0 \leq x \leq 1$) composition", *Journal of Applied Physics*, ***104***, 113524 **(2008)**.

[27] G. Xia, J. L. Hoyt, M. Canonico, "Si–Ge interdiffusion in strained Si/strained SiGe heterostructures and implications for enhanced mobility metal-oxide-semiconductor field-effect transistors", *Journal of Applied Physics*, ***101***, 044901 **(2007)**.

[28] Y. Dong, "A Systematic Study of Silicon Germanium Interdiffusion for Next Generation Semiconductor Devices", 193

[29] F. Rozé, O. Gourhant, E. Blanquet, F. Bertin, M. Juhel, F. Abbate, C. Pribat, R. Duru, "Comparative Analysis of Growth Rate Enhancement and Ge Redistribution during Silicon-Germanium Oxidation by Rapid Thermal Oxidation", *ECS Trans.*, ***75***, 67 **(2016)**.

[30] H. K. Liou, P. Mei, U. Gennser, E. S. Yang, "Effects of Ge concentration on SiGe oxidation behavior", *Applied Physics Letters*, ***59***, 1200 **(1991)**.

[31] F. K. LeGoues, R. Rosenberg, T. Nguyen, F. Himpsel, B. S. Meyerson, "Oxidation studies of SiGe", *Journal of Applied Physics*, ***65***, 1724 **(1989)**.

[32] S. Margalit, A. Bar-Lev, A. B. Kuper, H. Aharoni, A. Neugroschel, "Oxidation of silicon-germanium alloys", *Journal of Crystal Growth*, ***17***, 288 **(1972)**.

[33] R. Kube, H. Bracht, J. L. Hansen, A. N. Larsen, E. E. Haller, S. Paul, W. Lerch, "Composition dependence of Si and Ge diffusion in relaxed Si1−xGex alloys", *Journal of Applied Physics*, ***107***, 073520 **(2010)**.

[34] R. Kube, H. Bracht, J. Lundsgaard Hansen, A. Nylandsted Larsen, E. E. Haller, S. Paul, W. Lerch, "Simultaneous diffusion of Si and Ge in isotopically controlled heterostructures", *Materials Science in Semiconductor Processing*, ***11***, 378 **(2008)**.

[35] A. Atkinson, "Interfacial Diffusion", *MRS Online Proceedings Library*, ***122***, 183 **(1988)**.

[36] M. Ogino, Y. Oana, M. Watanabe, "The Diffusion Coefficient of Germanium in Silicon", *physica status solidi (a)*, ***72***, 535 **(1982)**.

[37] N. L. Rowsey, D. M. Fleetwood, B. R. Tuttle, S. T. Pantelides, "A Quantitative Model for ELDRS and H2 Degradation Effects in Irradiated Oxides Based on First Principles Calculations", 9

[38] S. N. Rashkeev, D. M. Fleetwood, R. D. Schrimpf, S. T. Pantelides, "Dual behavior of H+ at Si–SiO2 interfaces: Mobility versus trapping", *Applied Physics Letters*, ***81***, 1839 **(2002)**.

[39] T. Shimura, Y. Okamoto, T. Inoue, T. Hosoi, H. Watanabe, "Residual order in the thermal oxide of a fully strained SiGe alloy on Si", *Physical Review B*, ***81***, **(2010)**.

[40] D. Yu, G. S. Hwang, "Structure and Dynamics of Ge in the Si–SiO[sub 2] System: Implications for Oxide-Embedded Ge Nanoparticle Formation", *Electrochemical and Solid-State Letters*, ***11***, P17 **(2008)**.

[41] K. Hirose, H. Nohira, K. Azuma, T. Hattori, "Photoelectron spectroscopy studies of SiO2/Si interfaces", *Progress in Surface Science*, ***82***, 3 **(2007)**.

[42] I. Jiminez, "Influence of Si oxidation methods on the distribution of suboxides at Si/SiO2 interfaces and their band alignment: a synchrotron photoemission study", *Surface Science*, 7 **(2001)**.

[43] F. Rochet, C. Poncey, G. Dufour, H. Roulet, C. Guillot, F. Sirotti, "Suboxides at the Si/SiO2 interface: a Si2p core level study with synchrotron radiation", *Journal of Non-Crystalline Solids*, ***216***, 148 **(1997)**.

[44] D. Yu, G. S. Hwang, T. A. Kirichenko, S. K. Banerjee, "Structure and diffusion of excess Si atoms inSiO2", *Physical Review B*, ***72***, **(2005)**.

[45] A. H. Edwards, P. A. Schultz, H. P. Hjalmarson, "Spontaneous ionization of hydrogen atoms at theSi−SiO2interface", *Physical Review B*, ***69***, **(2004)**.

[46] P. A. Schultz, "Theory of Defect Levels and the “Band Gap Problem” in Silicon", *Physical Review Letters*, ***96***, **(2006)**.

[47] P. A. Schultz, "Charged Local Defects in Extended Systems", *Physical Review Letters*, ***84***, 1942 **(2000)**.

[48] N. L. Anderson, R. Pramod Vedula, P. A. Schultz, R. M. V. Ginhoven, A. Strachan, "Defect level distributions and atomic relaxations induced by charge trapping in amorphous silica", *Applied Physics Letters*, ***100***, 172908 **(2012)**.

[49] N. L. Anderson, R. P. Vedula, P. A. Schultz, R. M. Van Ginhoven, A. Strachan, "First-Principles Investigation of Low EnergyE′Center Precursors in Amorphous Silica", *Physical Review Letters*, ***106***, **(2011)**.

DISTRIBUTION

Email—Internal

Name	Org.	Sandia Email Address
Andrew Baczewski	01425	adbacze@sandia.gov
Quinn Campbell	01425	qcampbe@sandia.gov
Peter Schultz	01444	paschul@sandia.gov
Ping Lu	01819	plu@sandia.gov
Paul Sharps	01876	psharps@sandia.gov
George Wang	01876	gtwang@sandia.gov
Jeffrey Nelson	01880	jsnelso@sandia.gov
Keshab Sapkota	01882	krsapko@sandia.gov
Technical Library	01977	sanddocs@sandia.gov

Email—External [redacted]

Name	Company Email Address	Company Name
Kevin S. Jones	kjones@eng.ufl.edu	University of Florida
Chappel Sharrock	c.sharrock@ufl.edu	University of Florida
Emily Turner	emilymturner@ufl.edu	University of Florida

This page left blank

This page left blank

Sandia National Laboratories

Sandia National Laboratories is a multimission laboratory managed and operated by National Technology & Engineering Solutions of Sandia LLC, a wholly owned subsidiary of Honeywell International Inc. for the U.S. Department of Energy's National Nuclear Security Administration under contract DE-NA0003525.